electronics

MDPI

Article

An Accelerated Time-Domain Iterative Physical Optics Method for Analyzing Electrically Large and Complex Targets

Tai-Ping Sun, Zhou Cong, Zi He and Dazhi Ding *

Department of Communication Engineering, Nanjing University of Science and Technology, Nanjing 210094, China
* Correspondence: dzding@njust.edu.cn

Abstract: A local area coupling-based time-domain iterative physical optics (TD-LIPO) method for the analysis of the scattering from electrically large and complex targets is proposed in this study. A modulated Gaussian-pulse plane wave is taken as the incident wave. Initially, via a ray-tracing mechanism, the current radiation iteration is limited to the local area, and the iteration times are determined by the bounce times. This approach can lower the enormous computation time. In addition, GPU parallel technology is also applied to accelerate the method. Finally, the TD-LIPO method is used to obtain the scattering echo data matrix of the target under different radar observation angles. An inverse fast Fourier transform (IFFT) is performed on the matrix to obtain the ISAR image under a small bandwidth and small angle. Numerical examples and ISAR images show that the accelerated local area coupling technique can significantly improve computational efficiency and verify feasibility in radar imaging.

Keywords: electromagnetic scattering; time-domain (TD); iterative physical optics (IPO); GPU parallel; inverse synthetic aperture radar (ISAR)

Citation: Sun, T.-P.; Cong, Z.; He, Z.; Ding, D. An Accelerated Time-Domain Iterative Physical Optics Method for Analyzing Electrically Large and Complex Targets. *Electronics* **2023**, *12*, 59. https://doi.org/10.3390/electronics12010059

Academic Editor: Giovanni Riccio

Received: 30 October 2022
Revised: 2 December 2022
Accepted: 14 December 2022
Published: 23 December 2022

1. Introduction

In recent years, with the application of short-pulse and UWB communication in radar detection, target recognition and ground object remote sensing, the calculation and analysis of target time-domain electromagnetic scattering have become hotspots in computational electromagnetism [1–4]. The most commonly applied methods to accurately analyze the scattering characteristics of the target in the time-domain include the finite-difference time-domain (FDTD) method, integral equation time-domain (TDIE) method and finite element time-domain (FETD) method, which are time-domain numerical methods [5–8]. The time-domain numerical method is characterized by high accuracy and can be employed to solve for the accurate electromagnetic scattering of complex shapes and materials. Nevertheless, due to the large amount of iterative calculations, it cannot be used to explore electrically large objects, as it is limited by computer performance and computation time.

Time-domain high-frequency methods are demonstrated to be effective ways to address the problem. The most commonly used time-domain high-frequency methods are time-domain geometric diffraction, time-domain physical optics (TDPO) and time-domain equivalent edge current (TDEEC). In 1951, Keller proposed the geometric diffraction theory (GTD). He solved the problem of geometric optics failing when a target surface is discontinuous [9]. The time-domain expression of a conductor's straight split was initially derived from reference [10] and the time-domain expression of a more general curved split was later derived from reference [11]. However, the time-domain geometric diffraction theory and its frequency-domain version fail in the caustic region. The physical optics method can effectively overcome these existing defects. In 1994, time-domain physical optics (TDPO) was proposed by exploring reflector antennas in the literature [12]. A. Altintas and P. Russer [13] obtained the time-domain equivalent edge current (TDEEC) by applying an

inverse Fourier transform to the EEC expression. At present, numerous domestic scholars have carried out a lot of work on the time-domains of high frequencies. L. wei and Y. lingxia et al. [14,15] applied TDPO to investigate the electromagnetic scattering of electrically large targets and combined TDPO with FDTD to study composite targets [16].

In this paper, based on the IPO [17] theory, the TDIPO method is proposed to solve the time-domain scattering problem of electrically large and complex targets. By continuously updating the surface electromagnetic current, the coupling effect of electromagnetic waves on the target is well simulated. Subsequently, a local coupling method is proposed to lower the computational unknowns. Firstly, the number of iterations is determined by the number of bounces during ray tracing. Secondly, the current radiation iterations are limited to the local region around an intersected facet on the "bounce" path. After that, a GPU [18] with a high parallel-computing capability is used to improve the efficiency of the algorithm. Finally, an IFFT is performed on the echo data matrix received by GPU-TD-LIPO to obtain the ISAR image of the target.

2. Materials and Methods

2.1. Iterative Physical Optics and Time-Domain Iterative Physical Optics (TDIPO)

By the tangent plane approximation method, the equivalent electromagnetic flow generated by plane waves directly irradiating on the object can be obtained. The total scattered field at the tangent plane can be considered as the sum of the incident and reflected fields. We decompose the electromagnetic field into horizontal and vertical polarizations, which are defined as shown below:

$$\hat{q}_i = \frac{\hat{k}_i \times \hat{n}_i}{\left|\hat{k}_i \times \hat{n}_i\right|} \tag{1}$$

$$\hat{p}_i = \hat{q}_i \times \hat{k}_i \tag{2}$$

where $\hat{k}_i$ is the incident direction and $\hat{n}_i$ is the unit normal vector of the incident surface element. $\hat{q}_i$ is the vertical polarization direction perpendicular to the incident plane and $\hat{p}_i$ is the horizontal polarization direction parallel to the incident plane. According to Maxwell's boundary conditions, the Fresnel reflection coefficient formula can be obtained [19] as:

$$R^{TM} = \frac{\varepsilon_2 \cos\theta_i - \sqrt{\varepsilon_1\varepsilon_2 - \varepsilon_1^2 \sin^2\theta_i}}{\varepsilon_2 \cos\theta_i + \sqrt{\varepsilon_1\varepsilon_2 - \varepsilon_1^2 \sin^2\theta_i}} \tag{3}$$

$$R^{TE} = \frac{\sqrt{\varepsilon_1}\cos\theta_i - \sqrt{\varepsilon_2 - \varepsilon_1 \sin^2\theta_i}}{\sqrt{\varepsilon_1}\cos\theta_i + \sqrt{\varepsilon_2 - \varepsilon_1 \sin^2\theta_i}} \tag{4}$$

where $\cos\theta_i = -\hat{k}_i \cdot \hat{n}$. ε_1 and ε_2 denote the dielectric constants of the different media above and below, respectively.

Then the first-order induced electromagnetic current [20] on the target surface can be obtained as follows:

$$\boldsymbol{J}_0(\boldsymbol{r}) = \hat{n} \times \boldsymbol{H} = \begin{bmatrix} -(1-R^{TE})(\hat{e}_i \cdot \hat{q}_i)(\hat{n} \cdot \hat{k}_i)\hat{q}_i \\ +(1+R^{TM})(\hat{e}_i \cdot \hat{p}_i)(\hat{n} \times \hat{q}_i) \end{bmatrix} \frac{E_0}{Z_0} e^{-ik\hat{k}_i \cdot r} \tag{5}$$

$$\boldsymbol{M}_0(\boldsymbol{r}) = -\hat{n} \times \boldsymbol{E} = -\begin{bmatrix} (1+R^{TE})(\hat{e}_i \cdot \hat{q}_i)(\hat{n} \times \hat{q}_i) \\ +(1-R^{TM})(\hat{e}_i \cdot \hat{p}_i)(\hat{n} \cdot \hat{k}_i)\hat{q}_i \end{bmatrix} E_0 e^{-ik\hat{k}_i \cdot r} \tag{6}$$

In formulas (5) and (6), $\hat{e}_i$ and E_0 are the direction and amplitude of the incident electric field, respectively. $\boldsymbol{E}$ and $\boldsymbol{H}$ are the total electric field and total magnetic field, respectively.

According to Huygens' principle [21], the coupling field between the targets can be expressed by the following equations:

$$\boldsymbol{E}_1(\boldsymbol{r}) = \int_s \left[i\omega\mu \overline{\overline{G}}(\boldsymbol{r},\boldsymbol{r}') \cdot \boldsymbol{J}_0(\boldsymbol{r}') - \nabla \times \overline{\overline{G}}(\boldsymbol{r},\boldsymbol{r}') \cdot \boldsymbol{M}_0(\boldsymbol{r}') \right] ds\prime \tag{7}$$

$$\boldsymbol{H}_1(\boldsymbol{r}) = \int_s \left[i\omega\varepsilon \overline{\overline{G}}(\boldsymbol{r},\boldsymbol{r}') \cdot \boldsymbol{M}_0(\boldsymbol{r}') + \nabla \times \overline{\overline{G}}(\boldsymbol{r},\boldsymbol{r}') \cdot \boldsymbol{J}_0(\boldsymbol{r}') \right] ds\prime \tag{8}$$

where $\boldsymbol{J}_0(\boldsymbol{r}')$ and $\boldsymbol{M}_0(\boldsymbol{r}')$ are the first-order induced electromagnetic current of formulas (5) and (6). $\boldsymbol{E}_1(\boldsymbol{r})$ is the radiation electric field at a distance of r from the electromagnetic current source. $\boldsymbol{H}_1(\boldsymbol{r})$ indicates the radiation magnetic field. $\boldsymbol{r}$ is the position of the field point and $\boldsymbol{r}'$ is the position of the source point. $s\prime$ is the integration variable. $\overline{\overline{G}}(\boldsymbol{r},\boldsymbol{r}')$ is dyadic Green's function; the specific expressions are as follows:

$$\overline{\overline{G}}(\boldsymbol{r},\boldsymbol{r}') = \left(\overline{\overline{I}} + \nabla\nabla \frac{1}{k^2} \right) G(\boldsymbol{r},\boldsymbol{r}') \tag{9}$$

$$\nabla\nabla = \begin{bmatrix} \frac{\partial^2}{\partial x^2} & \frac{\partial^2}{\partial x \partial y} & \frac{\partial^2}{\partial x \partial z} \\ \frac{\partial^2}{\partial y \partial x} & \frac{\partial^2}{\partial y^2} & \frac{\partial^2}{\partial y \partial z} \\ \frac{\partial^2}{\partial z \partial x} & \frac{\partial^2}{\partial z \partial y} & \frac{\partial^2}{\partial z^2} \end{bmatrix}, \overline{\overline{I}} = \begin{bmatrix} 1\,0\,0 \\ 0\,1\,0 \\ 0\,0\,1 \end{bmatrix} \tag{10}$$

We posit $\boldsymbol{E}_1(\boldsymbol{r})$ in formula (7) as: $\boldsymbol{E}_1(\boldsymbol{r}) = \hat{e}_1 \boldsymbol{E}_1 \exp(ik\hat{k}_1 \cdot r)$. $\hat{e}_1$ and $\boldsymbol{E}_1$ are the direction and amplitude of the radiant electric field. $\hat{k}_1$ is the direction of the radiant electric field. $\hat{k}_1$ is substituted into formulas (1) and (2) to acquire $\hat{q}_1$ and $\hat{p}_1$. Then the second-order induced electromagnetic current on the target surface can be obtained as follows:

$$\boldsymbol{J}_1(\boldsymbol{r}) = \begin{bmatrix} -(1 - R^{TE})(\hat{e}_1 \cdot \hat{q}_1)(\hat{n} \cdot \hat{k}_1)\hat{q}_1 \\ +(1 + R^{TM})(\hat{e}_1 \cdot \hat{p}_1)(\hat{n} \times \hat{q}_1) \end{bmatrix} \frac{\boldsymbol{E}_1}{Z_0} e^{-ik\hat{k}_1 \cdot r} \tag{11}$$

$$\boldsymbol{M}_1(\boldsymbol{r}) = -\begin{bmatrix} (1 + R^{TE})(\hat{e}_1 \cdot \hat{q}_1)(\hat{n} \times \hat{q}_1) \\ +(1 - R^{TM})(\hat{e}_1 \cdot \hat{p}_1)(\hat{n} \cdot \hat{k}_1)\hat{q}_1 \end{bmatrix} \boldsymbol{E}_1 e^{-ik\hat{k}_1 \cdot r} \tag{12}$$

Then the iterations are repeated according to this rule until the accuracy requirements are met. The total induced electromagnetic current can be expressed as:

$$\boldsymbol{J}_{\text{total}}(\boldsymbol{r}) = \boldsymbol{J}_1(\boldsymbol{r}) + \boldsymbol{J}_2(\boldsymbol{r}) + \boldsymbol{J}_3(\boldsymbol{r}) + \ldots + \boldsymbol{J}_n(\boldsymbol{r}) \tag{13}$$

$$\boldsymbol{M}_{\text{total}}(\boldsymbol{r}) = \boldsymbol{M}_1(\boldsymbol{r}) + \boldsymbol{M}_2(\boldsymbol{r}) + \boldsymbol{M}_3(\boldsymbol{r}) \ldots \boldsymbol{M}_n(\boldsymbol{r}) \tag{14}$$

TDIPO are the time-domain version of IPO, obtained by performing the Fourier inverse transform (IFT) on the IPO.

$$\boldsymbol{J}_{\text{total}}(\boldsymbol{r},t) = \frac{1}{2\pi} \int [\boldsymbol{J}_{\text{total}}(\boldsymbol{r})] e^{i\omega t} d\omega \tag{15}$$

$$\boldsymbol{M}_{\text{total}}(\boldsymbol{r},t) = \frac{1}{2\pi} \int [\boldsymbol{M}_{\text{total}}(\boldsymbol{r})] e^{i\omega t} d\omega \tag{16}$$

Finally, under the far-field approximation condition [22], the target far-field scattered field can be obtained as:

$$\boldsymbol{E}_s(\boldsymbol{r},t) = -\frac{1}{4\pi r c} \int_s \hat{r} \times \left[\frac{\partial}{\partial t} \boldsymbol{M}_{\text{total}}(\boldsymbol{r}, t - \tau) - Z_0 \hat{r} \times \frac{\partial}{\partial t} \boldsymbol{J}_{\text{total}}(\boldsymbol{r}, t - \tau) \right] ds\prime \tag{17}$$

$$\boldsymbol{H}_s(\boldsymbol{r},t) = -\frac{1}{4\pi r c} \iint_s \hat{r} \times \left[\frac{\partial}{\partial t} \boldsymbol{J}_{\text{total}}(\boldsymbol{r}, t - \tau) + \frac{1}{Z_0} \hat{r} \times \frac{\partial}{\partial t} \boldsymbol{M}_{\text{total}}(\boldsymbol{r}, t - \tau) \right] ds\prime \tag{18}$$

where $\tau = (\hat{k}_i \cdot \boldsymbol{r}_0 + r - \hat{r} \cdot \boldsymbol{r}' + \left|\boldsymbol{r}' - \boldsymbol{r}_0\right|)/c$ is the total time delay. $\boldsymbol{r}_0$ is the initial incident point. $\hat{k}_i \cdot \boldsymbol{r}_0$ is the time delay caused by the incident pulse in the incident direction. $\boldsymbol{r}'$ is the point of ejection. $\hat{r} \cdot \boldsymbol{r}'$ is the time delay caused by the scattering pulse in the scattered direction. $|\boldsymbol{r}' - \boldsymbol{r}_0|$ is the distance between the field point and the source point. The above formulas use Gaussian integral.

2.2. Local Area Coupling-Based TDIPO (TD-LIPO)

For multi-reflection structures, the IPO method can consider the coupling effect by the iterative action of the current. In this method, the surface-induced current of the previous iteration is used as the source for radiation in each iteration. Unfortunately, the IPO method has a high time complexity of $O(n^2)$. In this article, a local area coupling approach is used to reduce the number of sources for iterations. For the target, the radiation field intensity of the surface current is related to the incident direction and its normal direction. Moreover, as the distance r between two points in Green's function increases, the radiation field intensity on the surface decreases gradually. Therefore, the radiation intensity in the direction of specular reflection is the largest, and gradually decreases with the side lobe direction. On this basis, the target can be truncated and only the coupling field in the local area of the surface is calculated.

In Figure 1, a model of dihedral angle with a side of one meter is displayed. The frequency of the incident wave is 10 GHz. The incident angle is $\theta_i = 45^\circ$, $\varphi_i = 0^\circ$. As shown in Figure 2, a model of a trihedral angle with a side of one meter is displayed. The frequency of the incident wave is 10 GHz. The incident angle is $\theta_i = 45^\circ$, $\varphi_i = 45^\circ$.

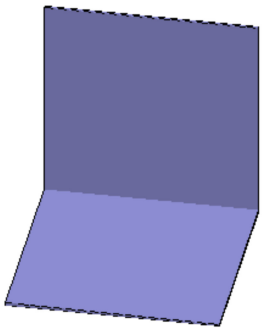

Figure 1. The dihedral angle model.

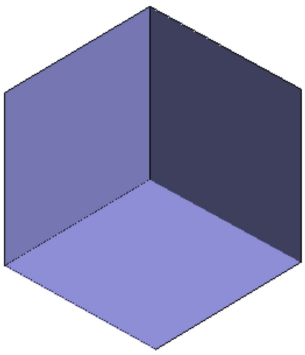

Figure 2. The trihedral angle model.

As shown in Figures 3 and 4, a triangular surface element (red triangle) on the model is selected for study. The colors on the graph indicate the normalized coupling intensity of the other triangles to the red triangle. On the ray tracing path, the surface elements in the local region contribute the most to the red triangle. The influence outside the local area gradually decreases. Thus, the iteration area of the red triangle can be restricted from the whole target area to a small local area. For the dihedral angle, there is only one local region

on the ray path with a large coupling effect on the red triangle, while for the trihedral angle, there are two local regions at an incident angle of $\theta_i = 45°$, $\varphi_i = 45°$. Thus, the dihedral angle needs only one iteration to reach convergence, while the trihedral angle needs two iterations. Considering the balance between efficiency and accuracy, the local region is set between 15 wavelengths and 20 wavelengths. It is important to note that surface elements that are not on the bouncing path are not processed by this method, i.e., processed with the IPO.

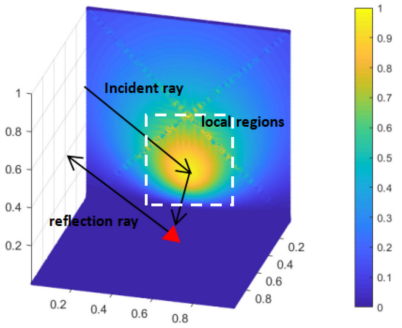

Figure 3. Normalized coupling intensity.

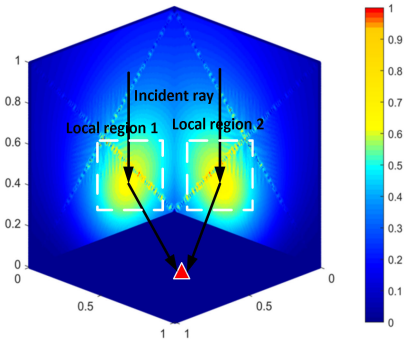

Figure 4. Normalized coupling intensity.

2.3. GPU Accelerated TD-LIPO Method

Since 2007, graphics card manufacturer NVIDIA has introduced CUDA, a parallel computing architecture based on GPU hardware. The number of stream multiprocessors (SMs) with computing power used in GPUs is generally hundreds or thousands, which is far more than the number of CPU cores. Therefore, parallel computing using GPUs has become an effective way to increase the speed of computation. This section performs parallel computation of TD-LIPO using CUDA based on GPU hardware platform.

Parallel computation of the TD-LIPO method can be understood as parallelism of the target surface elements. As shown in Figure 5, the model data are first read and pre-processed by the CPU module. Preprocessing is performed for each individual surface element, including discrimination of bright and shadow areas. At the same time, the solution of the reflective surface element is preprocessed. Then, the local coupling iterative solution of the surface elements is performed on the GPU. Finally, the scattering contributions of all surface elements are accumulated using the CPU module.

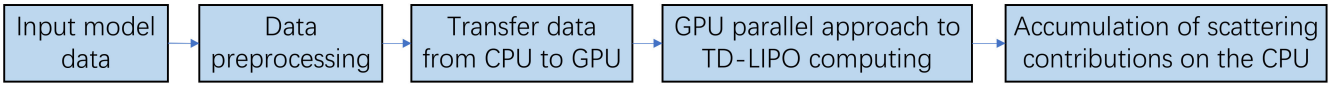

Figure 5. The process of algorithm implementation.

In the CUDA programming model, the CPU is called the host and the GPU is called the device. The device-side code is mainly used to perform parallel computing tasks. As shown

in Figure 6, each parallel code is called a kernel function, and each kernel function specifies a computational task. The kernel function is divided into three levels of parallelism: thread grid, thread block and thread. The maximum number of thread blocks allowed in each grid is 65,535. Each thread block contains multiple threads. Meanwhile, each thread and thread block has its own index.

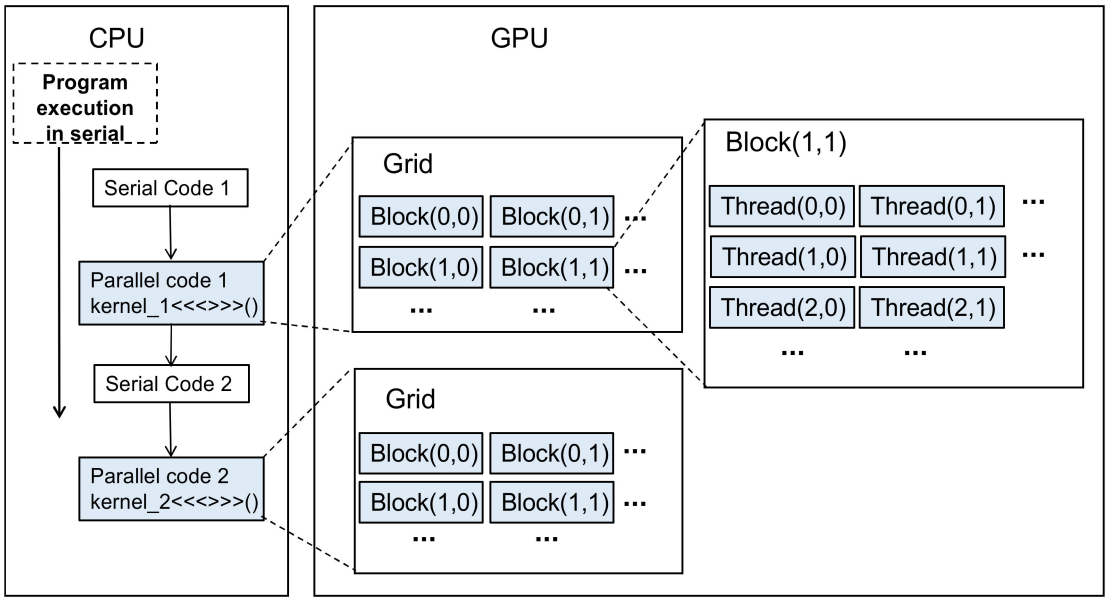

Figure 6. The structure of CUDA programming model.

In the Fortran program, the threads in the X-domain are marked by $(\text{blockIdx\%x} - 1) * \text{blockDim\%x} + \text{threadIdx\%x}$, where blockIdx%x is the number of the thread blocks and threadIdx%x is the number of the threads. Moreover, blockDim%x is the total number of threads in each thread block. As shown in Figure 7, the kernel function starts a thread grid containing three thread blocks and each thread block has four threads.

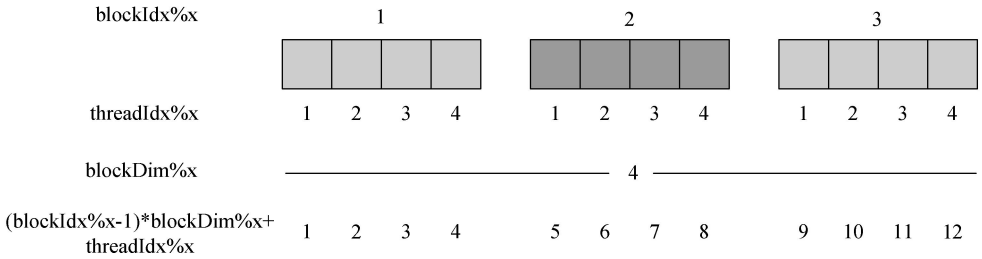

Figure 7. The indexing method of threads.

The maximum number of threads that SM can accommodate is related to the performance of the GPU. Additionally, the number of thread blocks and threads assigned to the SM has a significant impact on the GPU utilization. To effectively avoid the latency of thread waiting and to improve device utilization, the GPU needs to work at full capacity. The threads in the thread block are divided into groups for parallel tasks, and these groups are called warps. It is important to emphasize that warp is grouped into 32 units, so the number of threads in the thread block needs to be set to a multiple of 32 in order to obtain higher parallel computing efficiency.

The GPU used in this article is the NVIDIA GTX1080Ti. This GPU supports a maximum number of thread blocks per dimension of 1024, and the maximum number of threads that can fit within each thread block is also 1024. For the dihedral angle model of Section 3.2, Figure 8 counts the average computation time for different number of threads set in the

block. The average computation time is the result of multiple statistics of the total time the program runs divided by the total number of samples. The average computation time is shortest when the number of threads is 128. At this time, the program has the highest computational efficiency.

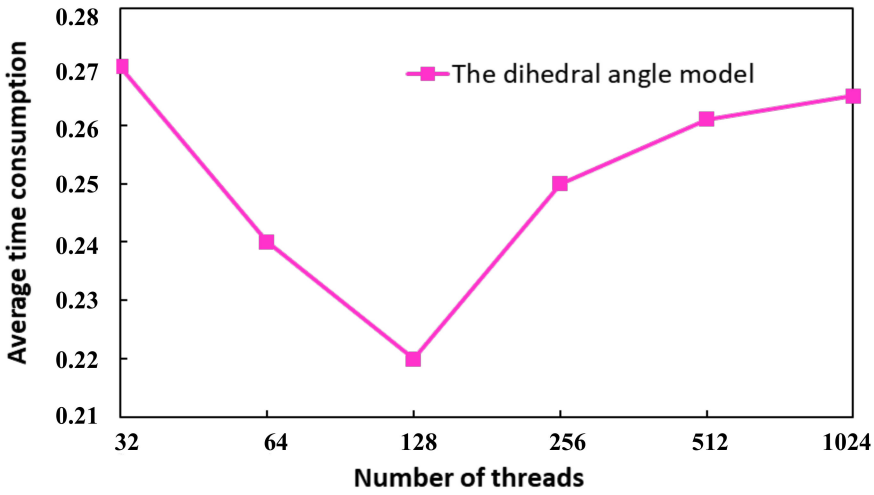

Figure 8. Thread index.

In this paper, only one thread grid is used and the number of threads per thread block is set to 128 for all cases involving GPU parallelism. The number of thread blocks can be calculated by the following formula:

$$N_{\text{thread blocks}} = ceiling(\frac{\text{Ntriangle}}{128}) \tag{19}$$

where Ntriangle is the number of triangles in which the target is meshed and *ceiling* means rounding up.

2.4. ISAR Imaging Based on GPU-TD-LIPO

At present, series of time-domain high-frequency algorithms are mature. Researchers have also made many valuable achievements in this field. In 2020, GUO linXin et al. [23] proposed an effective TDPO method for analyzing radar imaging of electrically large targets. However, the TDPO method considers only the single scattering of the incident wave on the object. The TDPO method for complex model imaging cannot consider the case of multiple coupling, which leads to a lack of information about the target features. The TDIPO method fully considers the multiple reflections between complex objects and can provide more accurate simulation images for target identification. Therefore, the TD-LIPO method is proposed for radar imaging of complex models. In addition, the GPU parallel computing method is used to further improve the imaging speed. This method is hereafter referred to as the GPU-TD-LIPO method.

By adopting the GPU-TD-LIPO method, the echo data matrix under small angle and small bandwidth can be obtained. The ISAR image of the target can be obtained by performing IFFT on the echo data matrix. In the time-domain response and broadband RCS calculation, the short-pulse signal is usually chosen as the time-domain excitation signal. The short-pulse signal has the advantages of less sampling points and wide frequency band range. Moreover, it also has many advantages in the application of UWB radar.

In this paper, modulated Gaussian pulse is used as the incident pulse wave. The modulated Gaussian pulse [24] can be expressed as follows:

$$\boldsymbol{E}_i(\boldsymbol{r}, t) = -\cos(2\pi f_0 t)\exp\left[-\frac{4\pi(t-t_0)^2}{{\tau_1}^2}\right]\hat{e}_i \tag{20}$$

where $\hat{e}_i$ is the direction of electric filed, and f_0 is the carrier frequency. τ_1 is the Gaussian waveform parameter. $t_p = 1.6\tau_1$ is the effective width of the pulse. t_0 is the time delay of the peak of the pulse and usually $t_0 = t_p/2 = 0.8\tau_1$.

When calculating the magnetic field, the relationship between the electric and magnetic fields in space can be used to solve for the value of the magnetic field, as follows:

$$\boldsymbol{H}_i(\boldsymbol{r}, t) = \frac{\hat{k}_i}{Z_0} \times \boldsymbol{E}_i(r, t) = -\cos(2\pi f_0 t) \exp\left[-\frac{4\pi(t - t_0)^2}{{\tau_1}^2}\right] \frac{\hat{k}_i \times \hat{e}_i}{Z_0} \tag{21}$$

where $\hat{k}_i$ is the direction of the incident wave and Z_0 is wave impedance.

The cross-range profile can be achieved by collecting the radar echoes from different views of the target. We assume that the radar scans a small angle $\Delta\varphi$ from φ_0 along the $\hat{\varphi}$. As shown in Figure 9, the incident direction $\hat{k}_i$ can be rewritten as:

$$\hat{k}_i = -\sin\theta_0 \cos(\varphi_0 + \Delta\varphi)\hat{e}_x - \sin\theta_0 \sin(\varphi_0 + \Delta\varphi)\hat{e}_y - \cos\theta_0 \hat{e}_z \tag{22}$$

In general, the selection of time sampling interval only needs to meet the Nyquist sampling criterion [25]. In each discrete time, the TD-LIPO method is used to calculate the time-domain response of the target. Moreover, the corresponding frequency-domain response sequence can be obtained by the discrete Fourier transform.

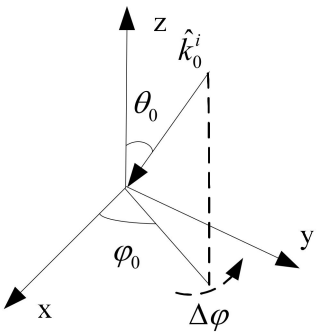

Figure 9. Incidence in small angle range.

The discrete Fourier transform pair has the following form.

$$F(\omega) = \Delta t \sum_{n=0}^{N} f(n\Delta t) e^{-j2\pi f \cdot n\Delta t} \tag{23}$$

$$f(t) = \Delta f \sum_{n=0}^{N} F(n\Delta f) e^{j2\pi n\Delta f \cdot t} \tag{24}$$

where N is the number of sampling points, Δt is the time interval, and Δf is the frequency interval.

Then, an echo matrix with small angle and small bandwidth can be obtained by collecting radar echoes from different viewing angles of the target. The two-dimensional inverse fast Fourier transform is applied to the matrix to obtain the image of the target.

3. Results

3.1. Performance of the IPO and Local Area Coupling IPO Method

Figure 10 shows a composite model of the rough surface and the ball, which are both ideal conductors. The size of the rough surface is 1.8 m × 1.8 m, the radius of the sphere is 0.15 m and the distance from the rough surface is 0.3 m. The unknown number is 132,816, the frequency is 4 GHz, the incident angle is $\theta_i = 30^\circ$, $\varphi_i = 0^\circ$, the observation angle is $\theta_s = -90 \sim 90^\circ$, $\varphi_s = 0^\circ$ and the polarization is vertical. The number of iterations for IPO

and Local IPO is two. The size of the local region is 15 wavelengths in Local IPO. RMSE is the root mean square error:

$$\mathrm{RMSE} = \sqrt{\frac{\sum_{i=1}^{n} \left(X_i - X_{benchmark,i}\right)^2}{n}} \tag{25}$$

where $X_{benchmark,i}$ is the benchmark, and X_i is the method compared to the benchmark.

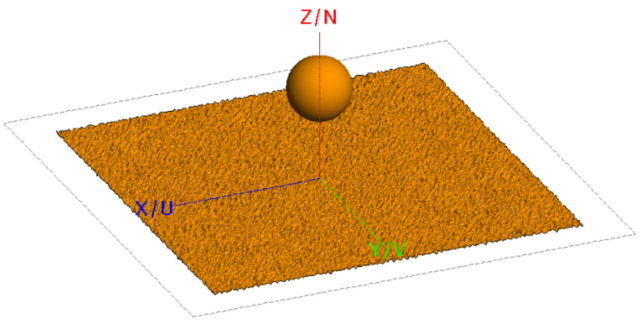

Figure 10. Rough surface and ball composite model.

Figure 11 shows the bistatic RCS results obtained by the MLFMA method in FEKO, the IPO and the proposed LIPO method. We can see that the results of three different methods are clearly close to each other especially in the vicinity from $-40\sim-20°$, which is the backward reflection directions. When the angle between the incident direction and the rough surface is very small, the calculation accuracy of the high-frequency method is not high. A simulation of this example is a finite rough surface: MLFMA calculates the edge effect at the edge of the finite rough surface and the LIPO temporarily does not consider the edge effect. Thus, there is a large error around 90° and $-90°$ in the LIPO and IPO. The result of MLFMA is used as a benchmark. We compare the computation time and the RMSE of the LIPO and IPO methods in Table 1. We can see that with a 0.5 dB error reduction, the LIPO is eight times faster than the IPO. The GPU parallel technology further increases the LIPO computation speed by up to 200 times. The result of GPU parallel technology is consistent with that of non-parallel technology.

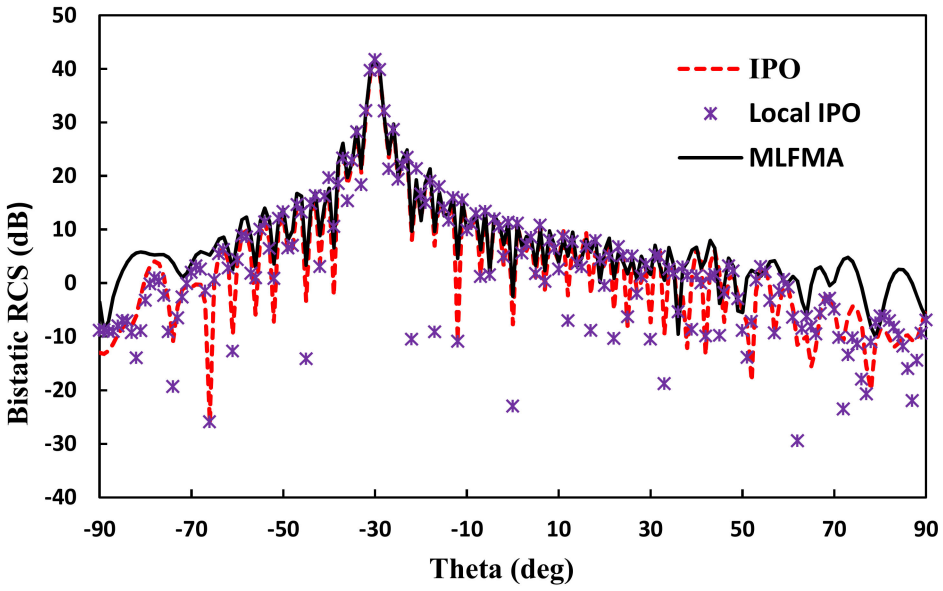

Figure 11. Bistatic RCS results for the composite model with different methods.

Table 1. The calculation time and accuracy of each algorithm.

Algorithm	Time (s)	Memory (MB)	RMSE (dB)
FEKO_MLFMA	6519	2069	Benchmark
IPO	2962	51	4.28
Local IPO	376	65	4.78
Local IPO + GPU	1.8	110	4.78

3.2. Performance of the TDIPO and TD-LIPO Method

The dihedral angle shown in Figure 12 is analyzed by the TD-LIPO method. The dihedral angle has a side of one meter. The unknown number is 135,112. The incident wave is a modulated Gaussian-pulse wave and the incident angle is $\theta_i = 45°$, $\varphi_i = 0°$. The center frequency is 2.5 GHz and the bandwidth is 3 GHz. The polarization is horizontal. Figure 12 shows the time-domain waveform of a Gaussian pulse. Figure 13 shows the time-domain echo response of the dihedral angle. Figure 14 is a comparison of RCS calculated by the different methods. The wavelength is calculated by using the highest frequency, 10 GHz. The number of iterations for IPO, TDIPO and TD-LIPO is one. In the experiment, the CPU was an Intel (R) Core (TM) i5-4590 CPU @3.30 GHz, and the GPU was an NVIDIA GTX1080Ti.

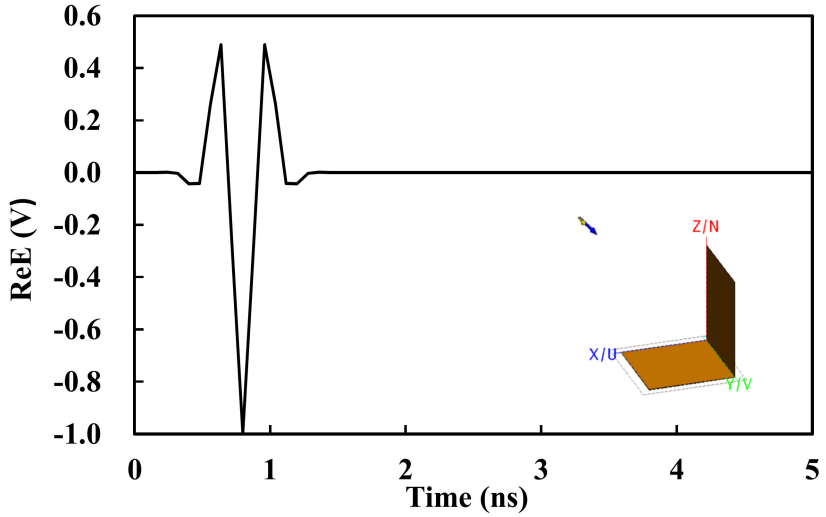

Figure 12. Time−domain waveform of incident pulse.

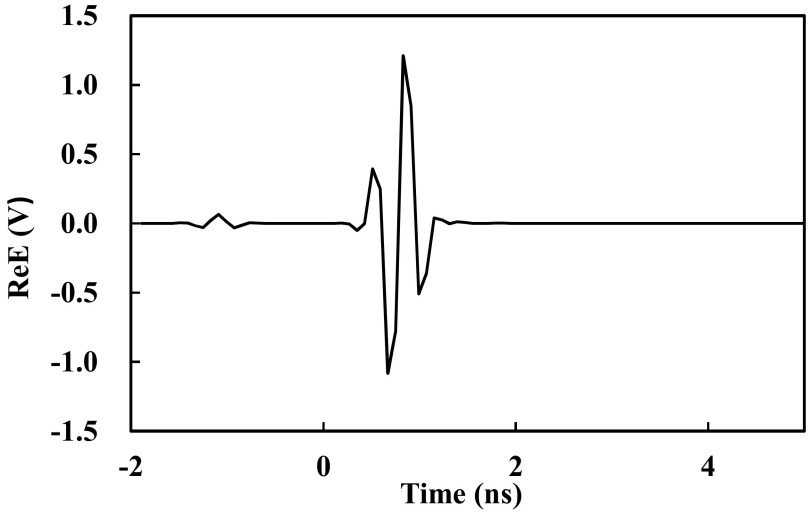

Figure 13. Time−domain response of dihedral angle based on TDIPO.

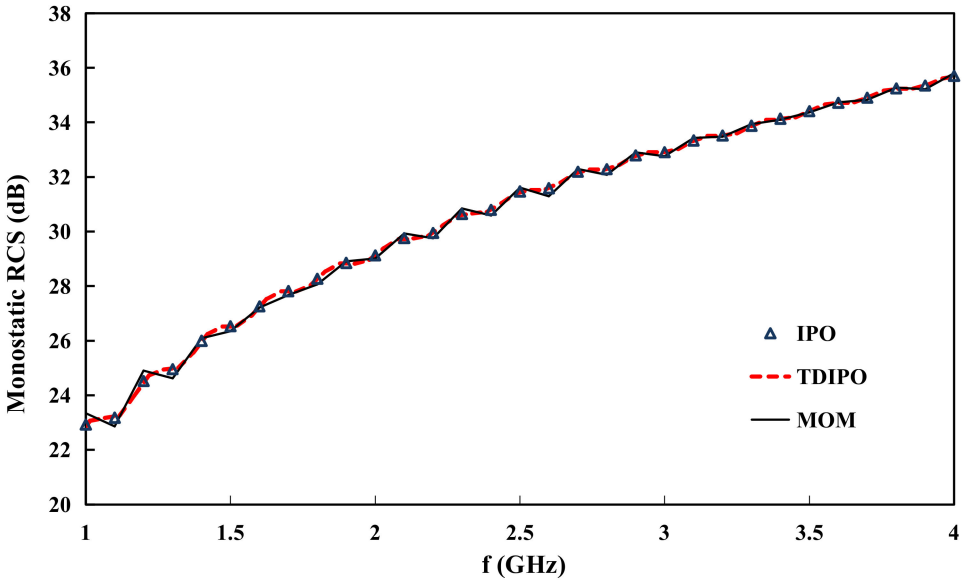

Figure 14. Monostatic RCS results for the dihedral angle model with different methods.

As shown in Figure 14, the IPO and TDIPO methods agree well with the MOM, proving the correctness of IPO and TDIPO in computing dihedral angles. The effect of different sizes of local areas on the accuracy of the TD-LIPO method is illustrated in Figure 15. The result of the MOM method is used as a benchmark. When the local area is set to five wavelengths, the error with the MOM method is the largest. As the local area gradually increases, the error gradually decreases. As can be seen from Table 2, the TDIPO method without local area coupling and GPU parallel acceleration takes nearly 4.18 h, which is unfavorable. With a parameter of five wavelengths, the TD-LIPO method is 7.2 times faster than TDIPO in terms of its calculation speed. However, this leads to large errors. In order to obtain a balance between time and accuracy, a local region between 15 and 20 wavelengths should selected. GPU parallel technology is also extremely effective at increasing speed.

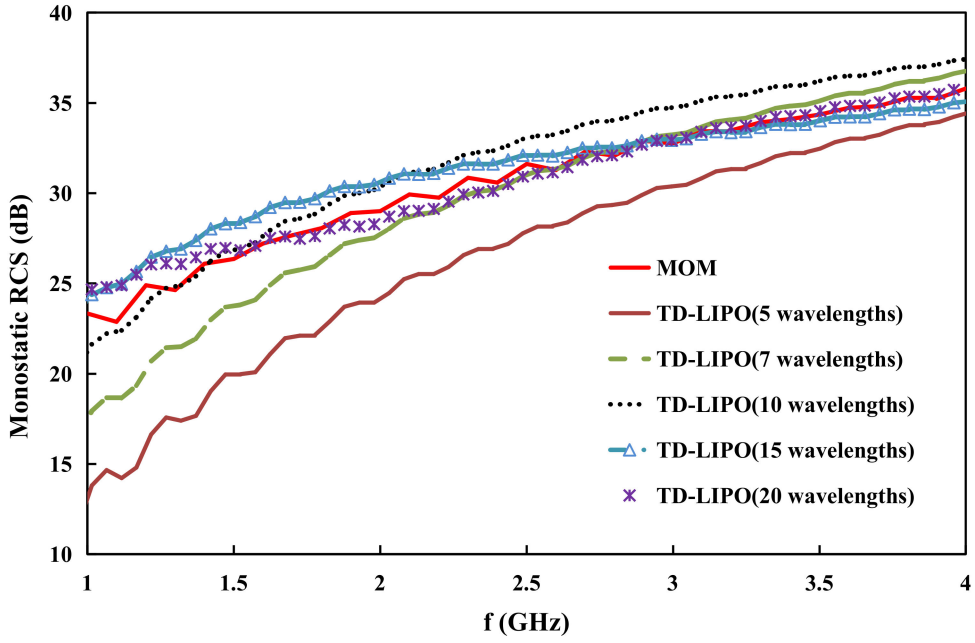

Figure 15. Monostatic RCS results for different size regions based on TD-LIPO method.

Table 2. The calculation time and accuracy of each algorithm.

Algorithm	CPU Time (s)	GPU Time (s)	RMSE (dB)
FEKO_MOM	23532	–	Benchmark
TD-LIPO (5 wavelengths)	2090	24.8	4.72
TD-LIPO (7 wavelengths)	2554	25.8	1.95
TD-LIPO (10 wavelengths)	3018	29.6	1.47
TD-LIPO (15 wavelengths)	3870	35.2	1.11
TD-LIPO (20 wavelengths)	9018	43.7	0.61
TDIPO (all wavelengths)	15064	48.5	0.18

3.3. ISAR Imaging Based on GPU-TD-LIPO

In all the following examples, the carrier frequency f_0 of the modulated Gaussian pulse is 5 GHz and the bandwidth is set to 2 G. The range resolution is 0.075 m and the azimuth resolution is 0.28 m. The following TDPO and TD-LIPO have all been added with GPU parallelism. In all the examples in this section, the size of the local region is set to 15 wavelengths. The wavelength is calculated by using the highest frequency, 10 GHz.

3.3.1. Study on ISAR Image of Dihedral Angle

The dihedral angle model in Section 3.2 is used for the study. The side length is 0.4 m. The unknown number is 22,324. The incident angle is $\theta_i = 45^\circ$ and the azimuth angle is $\varphi_i = 0^\circ$. The look angle of the radar varies from -3.0° to 3.0° around the center angle φ_i. The polarization is horizontal. The number of iterations for GPU-TD-LIPO is one.

Similarity represents the approximation between the two sets of data. The specific formula is as follows:

$$\text{Similarity} = \frac{\sum_i \sum_j [F(i,j) - \overline{F}][G(i,j) - \overline{G}]}{\left[\sum_i \sum_j [F(i,j) - \overline{F}]^2 \cdot \sum_i \sum_j [G(i,j) - \overline{G}]^2\right]^{1/2}} \tag{26}$$

where G is the matrix obtained by the MLFMA method. F is the matrix obtained by other methods. $\overline{G}$ and $\overline{F}$ are the means of G and F.

The ISAR images of the dihedral angle model are shown in Figure 16. Since the GPU-TDPO method does not take into account the bouncing coupling of the rays, two bright bands appear in Figure 16a. These two bright bands appear from the horizontal and vertical plates of the dihedral angle. Different from GPU-TDPO, the GPU-TD-LIPO method takes into account local coupling effects. The main contribution of electromagnetic wave scattering in the GPU-TD-LIPO method is in the mirror direction when considering the coupling between the two plates. All bounce contributions will appear in the same place on the image. Therefore, only one bright band appears on the Figure 16b. As can be seen from Table 3, GPU-TDPO takes less time than GPU-TD-LIPO but the similarity between GPU-TD-LIPO and MLFMA is much higher. Therefore, the GPU-TD-LIPO method has a greater advantage in target coupling imaging. Moreover, the dihedral angle can be equivalent to the strong scattering center.

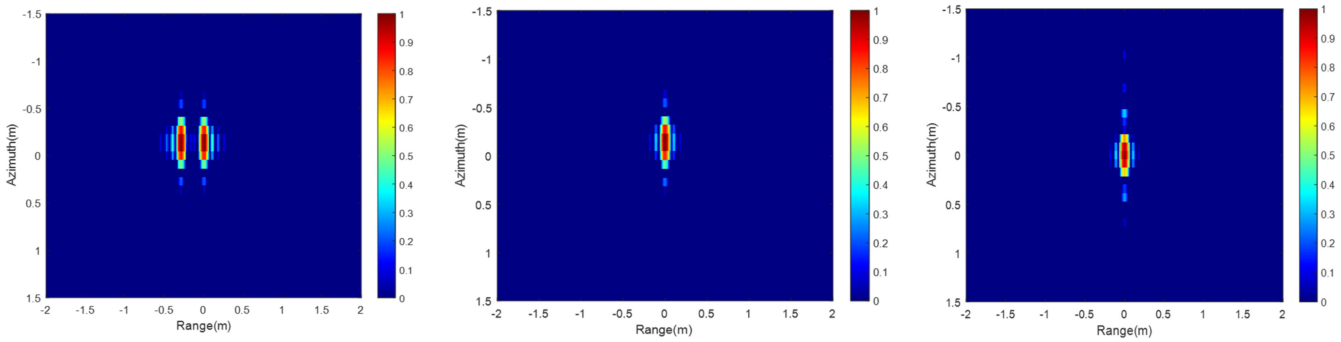

(**a**) (**b**) (**c**)

Figure 16. Normalized ISAR images of the dihedral angle under different methods. (**a**) TDPO; (**b**) TD−LIPO; (**c**) FEKO_MLFMA.

Table 3. Time and similarity of each method.

Algorithm	Time	Memory	Similarity
FEKO_MLFMA	20 h	1.4 GB	Benchmark
GPU-TDPO	20 s	78.5 MB	0.48
GPU-TD-LIPO	256 s	90 MB	0.95

3.3.2. Study on ISAR Image of Aircraft

The top and side views of the aircraft are shown in Figures 17 and 18. The size of the aircraft is 4.0 m × 3.5 m × 0.92 m. The unknown number is 677,408. The incident angle is $\theta_i = 60^\circ$ and the azimuth angle is $\varphi_i = 0^\circ$. The look angle of the radar varies from -3.0° to 3.0° around the center angle φ_i. The polarization is horizontal. The number of iterations for GPU-TD-LIPO is one.

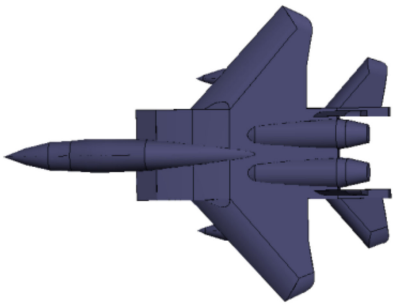

Figure 17. Top view of the model aircraft.

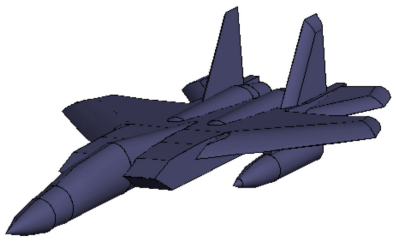

Figure 18. Side view of the model aircraft.

Comparing Figure 19a,b, it can be found that both the GPU-TDPO and GPU-TD-LIPO methods can present the basic shape of the aircraft. However, there are more highlights of the wing and tail in GPU-TD-LIPO, which is because it considers more coupling mechanisms than GPU-TDPO. As can be seen from Table 4, GPU-TD-LIPO takes almost six times longer than GPU-TDPO.

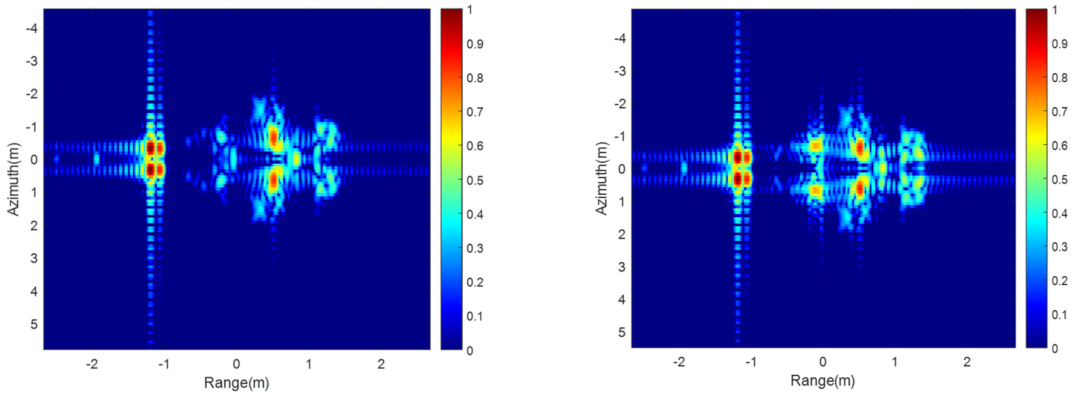

(**a**) (**b**)

Figure 19. Normalized ISAR images of the aircraft under different methods. (**a**) TDPO; (**b**) TD−LIPO.

Table 4. Time and memory of each method.

Algorithm	Time	Memory
GPU-TDPO	420 s	173.8 MB
GPU-TD-LIPO	2500 s	193.9 MB

3.3.3. Study on ISAR Image of Composite Scene

As shown in Figure 20, there is a ship on the rough surface. The size of the rough surface and the ship are 10 m × 10 m and 4 m × 1 m × 1.1 m, respectively. The unknown quantities of the ship and the rough surface are 449,446 and 500,000, respectively. The random rough surface here is generated using a Gaussian spectral density function, and the expression of the spectral density function for a two-dimensional Gaussian rough surface is: $W(k_x, k_y) = \delta^2 \frac{l_x l_y}{4\pi} \exp(-\frac{k_x^2 l_x^2 + k_y^2 l_y^2}{4})$, where δ represents the root mean square height, and l_x and l_y represent the correlation lengths of the random surface in the X and Y directions, respectively. k_x and k_y are the spatial wave numbers in the X and Y directions, respectively. Here $\delta = 0.01$ m and $l_x = l_y = 0.05$ m. The dielectric constant of the rough surface is $45 - 24.5$j. The incident angle is $\theta_i = 60^\circ$ and the azimuth angle is $\varphi_i = 90^\circ$. The look angle of the radar varies from 87.0° to 93.0° around the center angle φ_i. The polarization is vertical. The number of iterations for GPU-TD-LIPO is two.

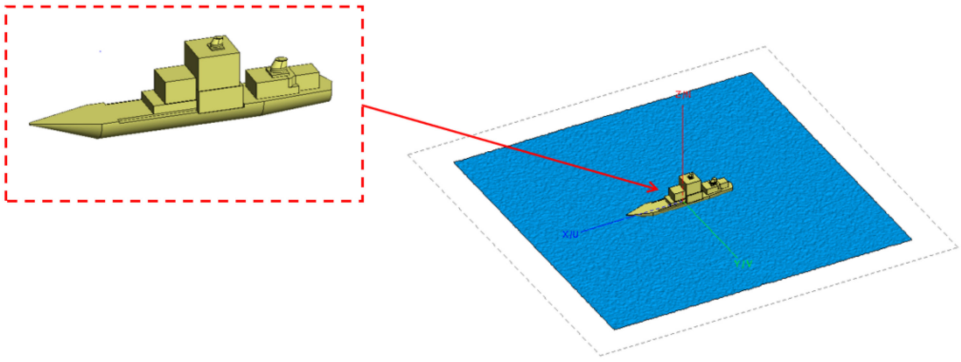

Figure 20. Composite model simulation of a ship at sea.

As shown in Table 5, the GPU-TD-PO method took 1.1 h and consumed 252.1 MB of memory. The GPU-TD-LIPO method took 2.6 h and consumed 264.2 MB of memory. The GPU-TD-LIPO method obtained more accurate imaging results and used some additional time and memory. As can be seen from Figure 21, since the side of the ship is smoother, the GPU-TDPO can also render the basic shape of the ship. However, there are more bright

spots on the rough surface and the coupling strength between the ship and the sea's surface is greater in GPU-TD-LIPO compared to that in the GPU-TDPO method.

Table 5. Time and memory of each method.

Algorithm	Time	Memory
GPU-TDPO	1.1 h	252.1 MB
GPU-TD-LIPO	2.6 h	264.2 MB

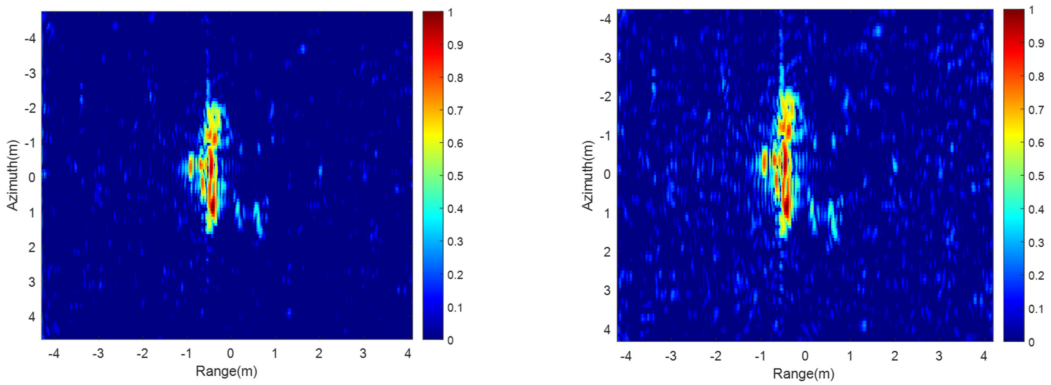

(**a**) (**b**)

Figure 21. Normalized ISAR images of the composite model under different methods. (**a**) TDPO; (**b**) TD−LIPO.

4. Conclusions

A novel local area coupling-based time-domain iterative physical optics (TD-LIPO) method is proposed for the analysis of scattering from electrically large and complex targets. The method considers multiple reflections between complex targets via local area iterations. This method reduces unnecessary coupling sources and saves significant computation time. Meanwhile, GPU parallelism is used to improve computational efficiency. Finally, using the proposed method, ISAR imaging of complex targets is investigated, and the results show more information and are more accurate than the traditional TDPO method. According to the numerical results, GPU-TD-LIPO is highly consistent with traditional TDIPO and the calculation speed is significantly improved.

Author Contributions: Conceptualization, T.-P.S. and Z.C.; methodology, Z.H. and D.D.; software, T.-P.S.; validation, T.-P.S., Z.C. and Z.H.; formal analysis, T.-P.S., Z.C., Z.H. and D.D.; investigation, T.-P.S.; resources, T.-P.S. and D.D.; data curation, T.-P.S.; writing—original draft preparation, T.-P.S.; writing—review and editing, T.-P.S., Z.C., Z.H. and D.D.; visualization, T.-P.S.; supervision, D.D.; project administration, D.D.; funding acquisition, D.D. All authors have read and agreed to the published version of the manuscript.

Funding: This work was supported in part by Natural Science 61931021, 61890541, 62025109, 62071231. Jiangsu Province Natural Science Foundation under Grant BK20211571, the Fundamental Research Funds for the Central Universities of No. 30921011207.

Data Availability Statement: No applicable.

Conflicts of Interest: The authors declare no conflict of interest.

References

1. Bennett, C.L.; Ross, G.F. Time-domain electromagnetics and its applications. *Proc. IEEE* **1978**, *66*, 299–318. [CrossRef]
2. Lui, H.S.; Shuley, N.V.Z. Radar Target Identification Using a "Banded" E-pulse Technique. *IEEE Trans. Antennas Propag.* **2006**, *54*, 3874–3881. [CrossRef]
3. Xie, D.X.; Tang, R.Y. Development of computational electromagnetics in China. *IEEE Trans. Magn.* **2006**, *42*, 509–514.

4. Shanker, B.; Ergin, A.A.; Aygun, K.; Michielssen, E. Analysis of transient electromagnetic scattering phenomena using a two-level plane wave time-domain algorithm. *IEEE Trans. Antennas Propag.* **2000**, *48*, 510–523. [CrossRef]
5. Capoglu, I.R.; Smith, G.S. A Total-Field/Scattered-Field Plane-Wave Source for the FDTD Analysis of Layered Media. *IEEE Trans. Antennas Propag.* **2008**, *56*, 158–169. [CrossRef]
6. Yee, K.S.; Shlager, K.; Chang, A.H. An algorithm to implement a surface impedance boundary condition for FDTD (EM scattering. *IEEE Trans. Antennas Propag.* **1992**, *40*, 833–837. [CrossRef]
7. Dyczij-Edlinger, R.; Peng, G.; Lee, J.F. Efficient finite element solvers for the maxwell equations in the frequency domain. Comput. *Methods Appl. Mech. Eng.* **1999**, *169*, 297–309. [CrossRef]
8. Li, G.S.; Liu, F.; Liu, J.B.; He, J.G. Method of TDIE for combination problems of electromagnetic field and circuit. *Propag. EM Theory* **2010**, *6*, 840–843.
9. Keller, J.B. Geometrical theory of diffraction. *J. Opt. Soc. Am.* **1962**, *52*, 116–130. [CrossRef]
10. Dey, S.; Mittra, R. A conformal finite-difference time-domain technique for modeling cylindrical dielectric resonators. *IEEE Trans. Microw. Theory Tech.* **1999**, *47*, 1737–1739.
11. Yu, W.H.; Mittra, R. A conformal finite difference time domain technique for modeling curved dielectric surfaces. *IEEE Microw. Wirel. Compon. Lett.* **2001**, *11*, 25–27.
12. Sun, E.Y.; Rusch, W.V.T. Time-domain physical-optics. *IEEE Trans. Antennas Propag.* **1994**, *42*, 9–15.
13. Altintas, A.; Russer, P. Time-domain equivalent edge currents for transient scattering. *IEEE Trans. Antennas Propag.* **2001**, *49*, 602–606. [CrossRef]
14. Yang, L.X.; Ge, D.B.; Wei, B. Time-Domain Physical-Optics Method for Transient Scattering Analysis. In Proceedings of the 2006 4th Asia-Pacific Conference on Environmental Electromagnetics, Dalian, China, 1–4 August 2006; pp. 861–864.
15. Luo, W.; Yin, W.Y.; Zhu, M.D.; Mao, J.F.; Zhao, J.Y. Investigation on Time- and Frequency-Domain Responses of Some Complex Composite Structures in the Presence of High-Power Electromagnetic Pulses. *IEEE Trans. Electromagn. Compat.* **2012**, *54*, 1006–1016. [CrossRef]
16. Yang, L.X.; Ge, D.B.; Wei, B. FDTD/TDPO hybrid approach for analyzing EM scattering by combinative objects. *Syst. Eng. Electron.* **2008**, *30*, 637–640.
17. Obelleiro-Basteiro, F.; Rodriguez, J.L.; Burkholder, R.J. An iterative physical optics approach for analyzing the electromagnetic scattering by large open-ended cavities. *IEEE Trans. Antennas Propag.* **1995**, *43*, 356–361. [CrossRef]
18. Kee, C.Y.; Wang, C.F. Efficient GPU Implementation of the High-Frequency SBR-PO Method. *IEEE Antennas Wirel. Propag. Lett.* **2013**, *12*, 941–944. [CrossRef]
19. Fung, A.K.; Li, Z.; Chen, K.S. Backscattering from a randomly rough dielectric surface. *IEEE Trans. Geosci. Remote Sens.* **1992**, *30*, 356–369. [CrossRef]
20. Rogier, H. Advanced applications of the field equivalence principle in numerical electromagnetic modelling techniques. *URSI Radio Sci. Bull.* **2003**, *305*, 22–29.
21. Eibert, T.F.; Hansen, V. 3-D FEM/BEM-hybrid approach based on a general formulation of Huygens' principle for planar layered media. *IEEE Trans. Microw. Theory Tech.* **1997**, *45*, 1105–1112. [CrossRef]
22. Miller, F.P.; Vandome, A.F.; Mcbrewster, J. *High Frequency Approximation*; Alphascript Publishing: Saarbrücken, Germany, 2010.
23. Guo, G.B.; Guo, L.X.; Wang, R. ISAR Image Algorithm Using Time-Domain Scattering Echo Simulated by TDPO Method. *IEEE Antennas Wirel. Propag. Lett.* **2020**, *19*, 1331–1335. [CrossRef]
24. Fallah, R.; Khorashadizadeh, S.M. Influence of Gaussian, Super-Gaussian, and Cosine-Gaussian Pulse Properties on the Electron Acceleration in a Homogeneous Plasma. *IEEE Trans. Plasma Sci.* **2018**, *46*, 2085–2090. [CrossRef]
25. Chardon, G.; Leblanc, A.; Daudet, L. Plate impulse response spatial interpolation with sub-Nyquist sampling. *J. Sound Vib.* **2011**, *23*, 5678–5689. [CrossRef]